nature photonics

Article

https://doi.org/10.1038/s41566-024-01579-9

Non-Hermitian hybrid silicon photonic switching

Received: 26 May 2024

Accepted: 14 October 2024

Xilin Feng[1], **Tianwei Wu**[2], **Zihe Gao**[2], **Haoqi Zhao**[1], **Shuang Wu**[2], **Yichi Zhang**[2], **Li Ge**[3,4] & **Liang Feng**[1,2] ✉

Leveraging the entire space of complex dielectric permittivity, non-Hermitian photonics has fundamentally altered wave propagation with complex optical potentials and has ushered in a host of new photonic applications. Through parity–time symmetry and its breaking—a delicate interplay between gain and loss—even the interaction between just two entities becomes counter-intuitive and intriguing. Here we realize, through hybrid III–V/Si integration, a scalable non-Hermitian switching network on a two-layer integrated photonic chip. Our platform is a hybrid, with a bottom silicon layer and a top InGaAsP layer that provides optical gain. By tuning the gain level in the top layer, vertically coupled waveguides operate below or above the exceptional point, where light is switched across two layers, among different input–output ports. For a single switching unit, the switching dynamics are ultrafast, on the order of 100 ps. In a large switching network, non-blocking and other diverse connectivities are established in single-wavelength and wavelength-selective switching, with high extinction ratios. Our approach adds scalable non-Hermitian switching to photonic design toolkits to simultaneously boost the switching time and bandwidth density to cutting-edge levels, therefore paving the way for compact and ultrafast monolithic integrated silicon photonics in next-generation optical information networks.

In today's era of data-intensive applications and high-speed communication, the demand for efficient and scalable optical interconnects has surged substantially across various domains such as data centres, telecommunications, high-performance computing and beyond. A key component of in-package input/output and co-packaged optics modules is an optical switch that is capable of real-time, high-speed routing and modulation of optical signals within integrated circuits, preferably enabling convenient integration into a silicon platform. Achieving these goals requires simultaneously addressing two primary technological challenges: rapid reconfigurability for high-speed routing; and an increased bit rate for modulated light input per unit area, accommodating a wider spectral bandwidth in a more compact footprint, that is, a greater data bandwidth density. Nevertheless, existing optical switch platforms are subject to limitations in one or more aspects, including speed, footprint, scalability or spectral bandwidth, which often result in an inability to simultaneously achieve a short switching time and a high bandwidth density.

Mach–Zehnder interferometers (MZIs)[1–4] and microring resonators (MRRs)[5–7] are the most prevalent building blocks in constructing silicon photonic networks. However, MZIs rely on two-arm interference which requires a π-phase modulation in one arm, often resulting in larger dimensions due to a limited change in the refractive index. Conversely, MRRs face bandwidth constraints that adversely impact their data processing capacity. Optical switches based on microelectromechanical systems, on the other hand, offer notable advantages in large-scale integration and design flexibility. However, owing to

---

[1]Department of Electrical and Systems Engineering, University of Pennsylvania, Philadelphia, PA, USA. [2]Department of Materials Science and Engineering, University of Pennsylvania, Philadelphia, PA, USA. [3]Department of Physics and Astronomy, College of Staten Island, CUNY, Staten Island, NY, USA. [4]The Graduate Center, CUNY, New York, NY, USA. ✉e-mail: fenglia@seas.upenn.edu

their intrinsically slow responses, their switching time is typically limited to a range of tens to hundreds of nanoseconds[8–12]. Semiconductor optical amplifier (SOA) switches based on III–V materials offer a fast switching speed and commendable bandwidth, but such switches often have a substantial device footprint and a high energy consumption[13–18]. Hence, there is a pressing need for the development of a completely new platform to break this switching time–bandwidth density trade-off and simultaneously push the boundaries on both fronts.

Here we address this challenge, using a silicon waveguide network with a heterogeneously integrated III–V semiconductor layer, to demonstrate hybrid silicon photonic switching by bringing in non-Hermiticity. Through such hybrid integration, waveguides in both layers are coupled, utilizing the broad gain spectrum of the III–V semiconductor. More importantly, through non-Hermitian tuning, the switching in our platform is now dictated by the non-Hermitian phase transition, exhibiting drastically different properties below and above the exceptional point due to distinctive characteristics associated with parity–time (PT) symmetry and its breaking[19–26]. By virtue of non-Hermiticity, three benefits arise: the spectral bandwidth of our switch spans a broad range of the III–V material's gain spectrum; the device footprint in our system is minimized to the coupling length, which enables complete power transfer between two PT symmetrically coupled waveguides; and the switching time, owing to the compact footprint, is also minimized, close to the III–V semiconductor's carrier lifetime. Together they constitute a scalable optical switching network with an ultrafast switching time and a high bandwidth density, capable of non-blocking signal routing and wavelength-selective switching (WSS) in a broad telecom spectrum. In contrast to traditional SOAs[13–18], our result highlights energy transfer between the III–V and silicon structures, not only marking a breakthrough in the large-scale integration of active gain elements on a silicon substrate with rich programmable functionalities but also an advance in experimental non-Hermitian physics.

The hybrid silicon photonic switching network (as demonstrated in Fig. 1a) is based on an 8 × 8 silicon waveguide grid array that incorporates low-loss waveguide crossings to minimize the cross-talk of light travelling in orthogonal directions in the silicon layer. In each switching unit, the transition of guided light from the horizontal (x) to the perpendicular (y) direction is achieved through a curved InGaAsP waveguide with a 90° bend heterogeneously integrated on top of the silicon waveguides. The coupling between the InGaAsP and silicon waveguides is controlled by an oxide layer (SiO_2) between them and further tuned by manipulating the gain of InGaAsP through optical pumping. It can facilitate the transfer of input light horizontally from the silicon waveguide to the InGaAsP waveguide, redirecting it perpendicularly, and subsequently dropping it to the silicon waveguide beneath. In this scenario, the effective Hamiltonian of the coupled InGaAsP–Si waveguides can be written as

$$H = \begin{pmatrix} \beta_1 & \kappa \\ \kappa & \beta_2 + ig \end{pmatrix}, \tag{1}$$

where β_1 is the real part of the wavevector of the guided mode in the silicon waveguide, β_2 is the real part of the wavevector of the guided mode in the InGaAsP waveguide, respectively, g represents the imaginary part of the wavevector in the InGaAsP waveguide (with $g > 0$ for gain and $g < 0$ for loss) and κ denotes the intrinsic coupling constant between the two waveguides, which is related to the thickness of the oxide layer. The imaginary index of silicon, compared with that of InGaAsP, is negligible and thus ignored in our derivation. To ensure that $\beta_1 = \beta_2 \equiv \beta_0$ (that is, no wavevector mismatch, where β_0 is the common real part of the wavevectors in the two waveguides) and to facilitate complete energy transfer between the two waveguides, the cross-sections of the waveguides are carefully designed: 600 × 250 nm for the silicon waveguide and 750 × 270 nm for the InGaAsP waveguide. With input from the silicon waveguide travelling along the x direction, the evolution of the optical mode in the two waveguides is

$$\begin{pmatrix} a_1(x) \\ a_2(x) \end{pmatrix} = \frac{e^{-i\beta_0 x} e^{\frac{gx}{2}}}{\cos\theta} \begin{bmatrix} \cos(qx - \theta) \\ -i\sin(qx) \end{bmatrix}, \tag{2}$$

where $a_1(x)$ is the electric field in the silicon waveguide and $a_2(x)$ is the electric field in the InGaAsP waveguide, and $\theta = -\sin^{-1}(g/2\kappa)$ and $q \equiv \kappa\cos\theta$. Note that θ (and q) are real (imaginary) in the PT-symmetric (PT-broken) phase, where $|g| < 2|\kappa|$ ($|g| > 2|\kappa|$).

In this coupled waveguide system, the non-Hermiticity (that is, g) controls the PT symmetry breaking of the system: $|g| < 2|\kappa|$ for the PT-symmetric phase and $|g| > 2|\kappa|$ for the PT-broken phase. In the absence of external pumping, InGaAsP is inherently lossy with $|g| > 2|\kappa|$, placing the system in the PT-broken phase where the two waveguides are effectively decoupled. In this state, the system remains 'off' with the input light staying in the silicon waveguide and travelling directly to the through port (Fig. 1b). External pumping on InGaAsP turns the material loss into gain, leading to a phase transition into the PT-symmetric phase with $|g| < 2|\kappa|$. In this state, the coupling between the two waveguides is 'on', enabling energy transfer between them (Fig. 1c). According to equation (2), the condition of $\cos(qx - \theta) = 0$ corresponds to complete power transfer from the silicon waveguide to the InGaAsP waveguide, defining the coupling length L needed between two waveguides: $L = \frac{\theta + \frac{\pi}{2}}{q} = 30\,\mu\text{m}$ (see Supplementary Section 1).

The hybrid silicon photonic switching network was fabricated using wafer bonding for the heterogeneous integration of InGaAsP with silicon, followed by overlay electron-beam lithography (Fig. 2a; see Methods and Extended Data Fig. 1). To minimize the reflection induced by a complex optical potential[27], both ends of the InGaAsP waveguide are tapered to ensure smooth mode transitions (see Supplementary Section 1 for details). The device was characterized using a pulsed input laser at a wavelength of 1,490 nm with a pulse duration of 10 ns, synchronized with the patterned illumination on the curved InGaAsP waveguide from a pump laser at a wavelength of 1,064 nm with a pulse duration of 20 ns. To achieve a high extinction ratio, the thickness of the oxide layer between the two waveguides must be meticulously designed. In the on state, its resultant intrinsic coupling (κ) is sufficiently high to facilitate energy transfer over a short distance, ensuring a compact device footprint for high-density integration. Conversely, in the off state, the large contrast in the imaginary index between silicon and InGaAsP reverses the effective coupling from κ, leading to a sufficiently low coupling strength to minimize modal loss despite the material loss of InGaAsP in the absence of pump. In our case with an oxide layer thickness of 325 nm, the transmission spectrum of a single switching unit, as a function of the pump power that shifts InGaAsP from loss to gain, exhibits high extinction ratios between the on and off states: 15 dB at the through port and 37 dB at the drop port (Fig. 2b; see Methods, Extended Data Fig. 2 and Supplementary Section 2 for more details). Note that in the on state, optical gain amplifies the mode resulting in an increased transmission to the drop port. Moreover, time-correlated measurements (see Methods, Extended Data Fig. 2 and Supplementary Section 3) show an ultrafast switching response (Δt, corresponding to the relative delay time in peak positions) on the order of 100 ps (Fig. 2c,d). As our photonic switching relies on the active excitation of carriers in InGaAsP, the response time is consistent with the carrier lifetime and rise time reported previously in the literature[28,29] and at least an order of magnitude faster than the current state-of-the-art optical switch array[1,3,8,9,11].

For our single switch units with the through ports cascading horizontally and the drop ports cascading vertically in two dimensions,

https://doi.org/10.1038/s41566-024-01579-9

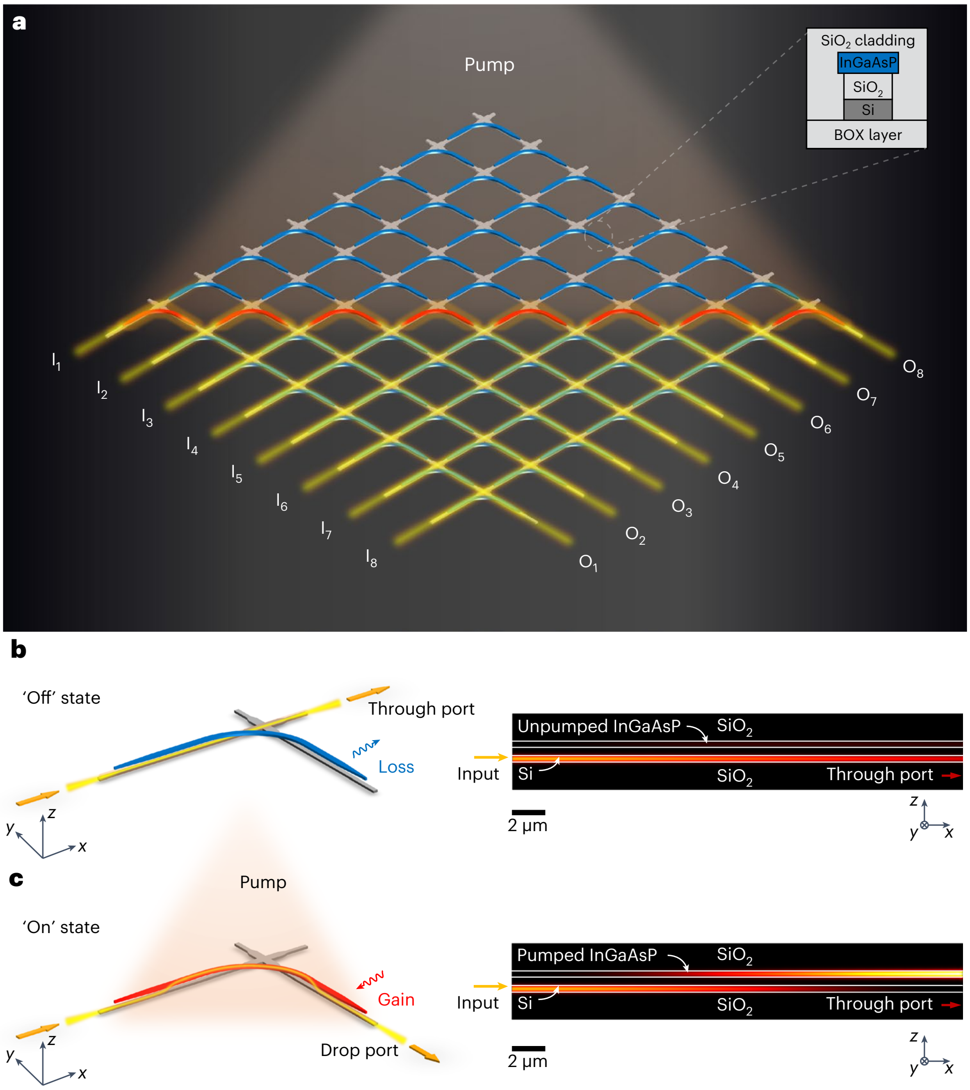

Fig. 1 | III–V/Si hybrid photonic switch. a, Schematic of the switch array. Silicon waveguides on the bottom layer are shown in grey, whereas the InGaAsP waveguides on the top layer are shown in blue (not pumped) or red (pumped). The pump pattern is depicted via the orange shading. The signal light (depicted with yellow shading) from each input port (I_1–I_8) is routed to the perpendicular direction at the pumped unit, then to the target output port (O_1–O_8). The inset shows the layer information of the waveguides in the coupling region. BOX, buried oxide. **b**, Working principle of a single switch unit in the 'off' state. In the left image, the InGaAsP waveguide is very lossy due to the absence of pump light, resulting in the system working in the PT-broken phase. Most of the light stays in the silicon layer and goes directly to the through port. The right image shows energy flow in the coupling region in the *x* direction. **c**, Working principle of a single switch unit in the 'on' state. The pump light provides gain to the InGaAsP waveguide on the top layer, resulting in the system operating in the PT-symmetric phase. In the left image, input light from the silicon waveguide on the bottom layer is coupled to the upper InGaAsP layer and then coupled back to the perpendicular bottom silicon layer, and finally travels to the drop port. The right image shows energy flow in the coupling region in the *x* direction before the crossing. In **b** and **c**, the scale bar represents the dimensions in the *x* direction, whereas the *z* direction has been stretched by a factor of 1.5 to better visualize the layer information.

we form our non-blocking switch network (Fig. 3). Switching and routing within the network is defined by the pumping strategy. An optical signal from a certain input port remains horizontal before it reaches the pumped switch, and remains vertical afterwards until it reaches the output port. Inside the pumped switch, non-Hermitian PT-symmetric hybrid waveguides bend the light downwards. To verify the non-blocking connectivity, we tested our switches in an 8 × 8 network (Fig. 3a) with an input wavelength of 1,490 nm. The L-shaped regions for optical pumping were generated via a spatial light modulator (SLM). We denote our input state across ports I_1 to I_8 by a vector with the Boolean intensity level (0 or 1) at each port, and we measured the signals across the eight output ports, O_1–O_8, using a monochromator (see Methods, Extended Data Fig. 2 and Supplementary Section 5 for experimental details). In Fig. 3b–d, we show images taken using a charge-coupled device (CCD) camera for three such vectors when the diagonal elements are pumped in the network. Strong signals from the desired output port(s) can be clearly seen, while the rest of the output ports stay dark. For 15 input vectors with one, four or all port(s) launched, we achieved port-to-port non-blocking switching for all of them, with only 3.1% average intensity cross-talk to the undesired ports (Fig. 3e; see Supplementary Section 5 for more information). We attribute this small cross-talk mainly to the unavoidable collection of the scattering light from the input port and the imperfect pump pattern generation from the SLM, where the pump region is blurred and the pump light oversteps its boundary with adjacent switch units. Furthermore, our switch network can be dynamically reconfigured with its non-blocking feature maintained, by redistributing the pump placements (Fig. 3f,g). The new input–output connectivity can also

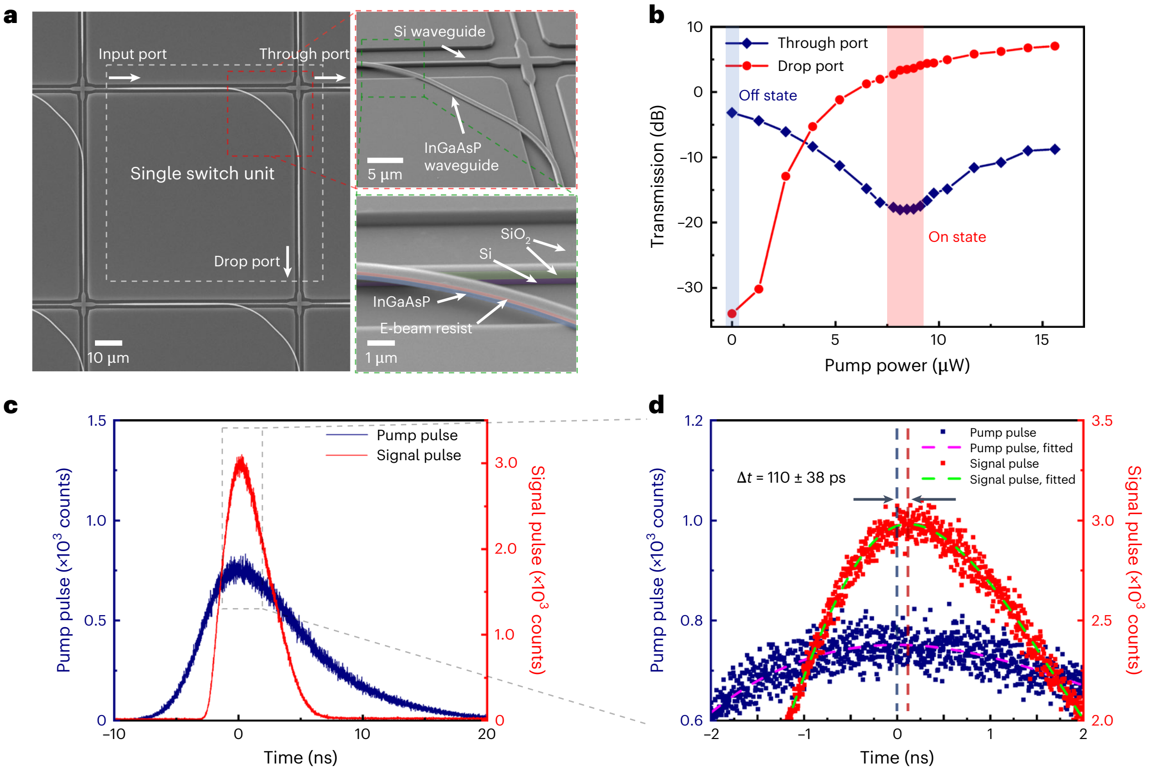

Fig. 2 | Characterization of a single switch unit. a, Scanning electron microscopy images of the switch. Left: a single switch unit (outlined by the white dashed box) in the switch array. Top right: expanded and tilted view of area highlighted by the red dashed square in the left image. Bottom right: false-colour image of the area highlighted by the green dashed square in the top-right image, expanded further to show the layer information. E-beam, electron-beam. **b**, Transmission of the through and drop ports as a function of the pump power. The working ranges of the on and off states are depicted by the red and blue shaded areas, respectively (see Supplementary Section 4 for a more detailed analysis on the insertion loss). **c**, Time response of a single switch unit measured via time-correlated single photon counting. The blue curve shows the pump pulse collected from the surface of the sample, and the red curve shows the signal pulse collected from the drop port, with a relative peak position delay of 110 ± 38 ps. The time zero is set to be the peak position of the pump pulse. **d**, Expanded view of the dashed box in **c**, showing the peak positions of the pump and signal pulses, highlighted by the vertical blue and red dashed lines, respectively.

be securely established, with minimal cross-talk (2.7% in Fig. 3f and 3.0% in Fig. 3g).

Incorporating spectral parallelism into our switch network, we next demonstrate WSS. Wavelength selectivity is introduced by adding MRRs with various spectral resonances to the input ports (Fig. 4a). With this design, each row in our network will now possess a distinct spectral component. For these experiments, we chose three wavelength (λ_{1-3}) values, at 1,470, 1,490 and 1,510 nm, a bandwidth that spans a broad range of 40 nm, leveraging the broad gain spectrum (see Supplementary Section 8) of active semiconductors for WSS. These spectral components were multiplexed and simultaneously launched into the switch network from a common input stream (Fig. 4a). Using the same pumping strategy as in Fig. 3, we first establish one-to-one non-blocking connectivity (Fig. 4b), where three wavelengths are switched among five outputs with an extinction ratio (the largest versus the second largest output port intensities at one wavelength) of over 17 dB for all wavelength components. More importantly, with the spectral orthogonality in WSS, more diverse connectivities can be realized by adopting more diverse pumping strategies. By pumping multiple switches within the same column, multiple inputs can now be switched and routed to the same output port (multiple-to-one), where different spectral components are well-separated using the spectrum measurement, with a minimum extinction ratio of 16 dB (Fig. 4c,d). One-to-multiple connectivity is also viable (Fig. 4e), through the wavevector mismatch between the waveguides in two layers. We can control the widths of the waveguides such that PT-symmetric pumping does not bring about complete power transfer to the top layer—non-trivial amount of power still resides in the bottom silicon layer, extending into subsequent switches and making one-to-multiple connectivity possible when multiple switches are pumped in the same row (see Supplementary Section 9). With a versatile pumping strategy, therefore, WSS in our switch network is equipped with a diverse, flexible and reconfigurable input–output connectivity.

We have demonstrated a non-Hermitian hybrid silicon photonic switch that is distinct from the existing models and has the potential to boost the on-chip data bandwidth density by around three orders of magnitude (see Supplementary Sections 8 and 10). In terms of the switching mechanism, non-Hermitian phase transition across the exceptional point determines the flow of light exiting the two-layer hybrid silicon switch unit. Compared with non-Hermitian mode switching between two states of the same Hamiltonian[30,31], the switching here in our work occurs between the PT-symmetric and -broken phases of two different Hamiltonians, dynamically tuned by the gain–loss parameter g. In particular, such continuous tunability across the PT phase diagram makes our platform ideal for studies with rich non-Hermitian physics, such as slow light at the exceptional point[32,33]. Of the many metrics for evaluating an optical switch, our switch excels in size and switching time, with a compact footprint of only 85 × 85 µm per unit and a switching time on the order of 100 ps, approaching the fundamental limit of the carrier lifetime and rise time in InGaAsP with full utilization of its broad spectral bandwidth. In a network with the large-scale and tunable non-Hermitian functionalities formed by our scalable switch, versatile pumping strategies generate diverse input–output connectivity, where an excellent extinction ratio is sustained across

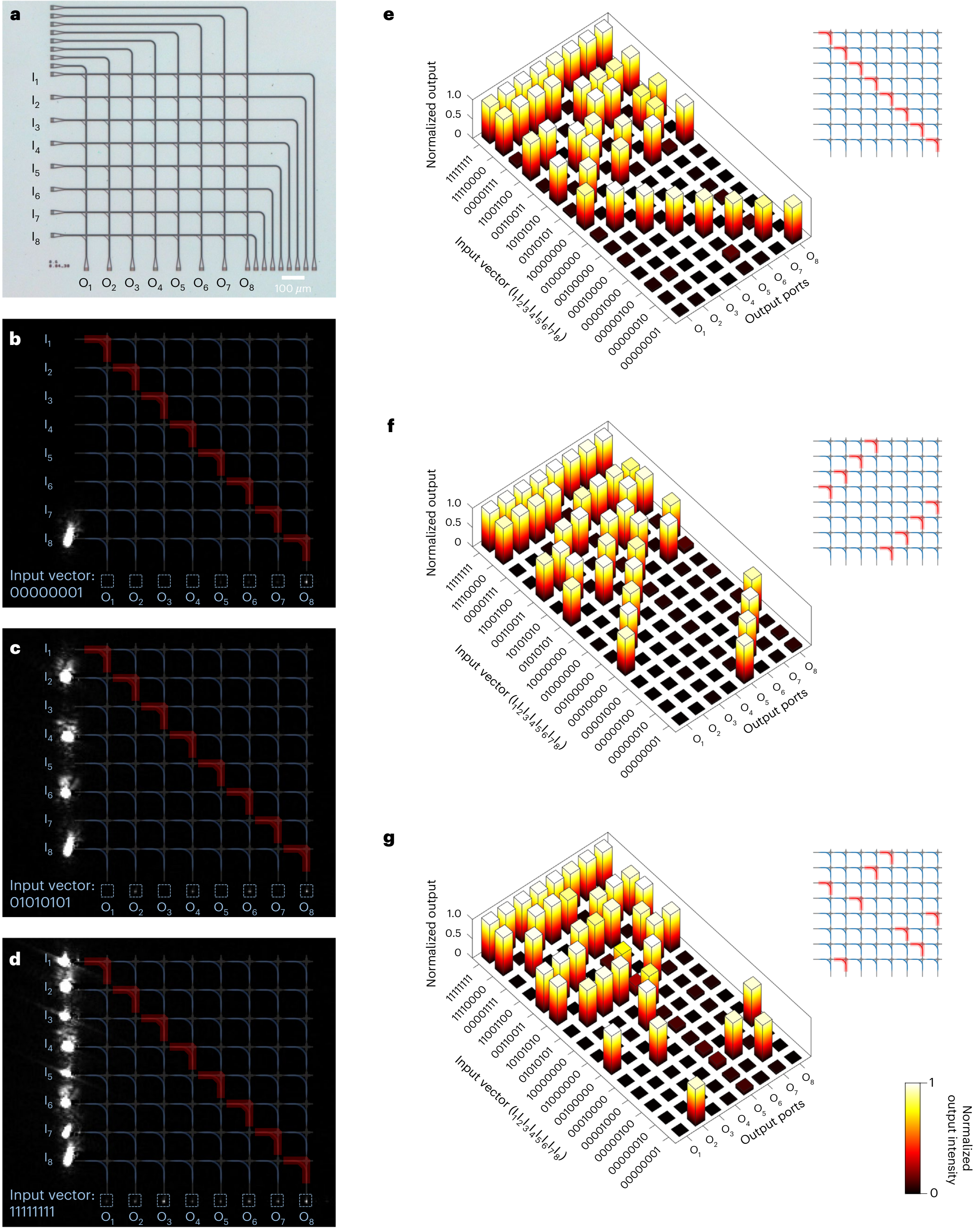

Fig. 3 | Characterization of an 8 × 8 switch. a, Optical microscope image of the 8 × 8 switch array. **b**–**d**, CCD image of the measurement with the diagonal pump but different input vectors: input vector 00000001 with an input only at port I_8 (**b**), input vector 01010101 with inputs at ports I_2, I_4, I_6 and I_8 (**c**) and input vector 11111111 with inputs at all of the ports (**d**). The intensity of photoluminescence has been subtracted. **e**–**g**, Output intensity measured at each output port (O_1–O_8) for three different pump patterns. Each output port is normalized individually across 15 different input vectors ($I_1I_2I_3I_4I_5I_6I_7I_8$). The inset in each figure shows the pump pattern (shaded in red). Our device architecture offers sufficient scalability, where our current 8 × 8 switching network can be fully scalable to a higher dimensionality (see, for example, Supplementary Section 6).

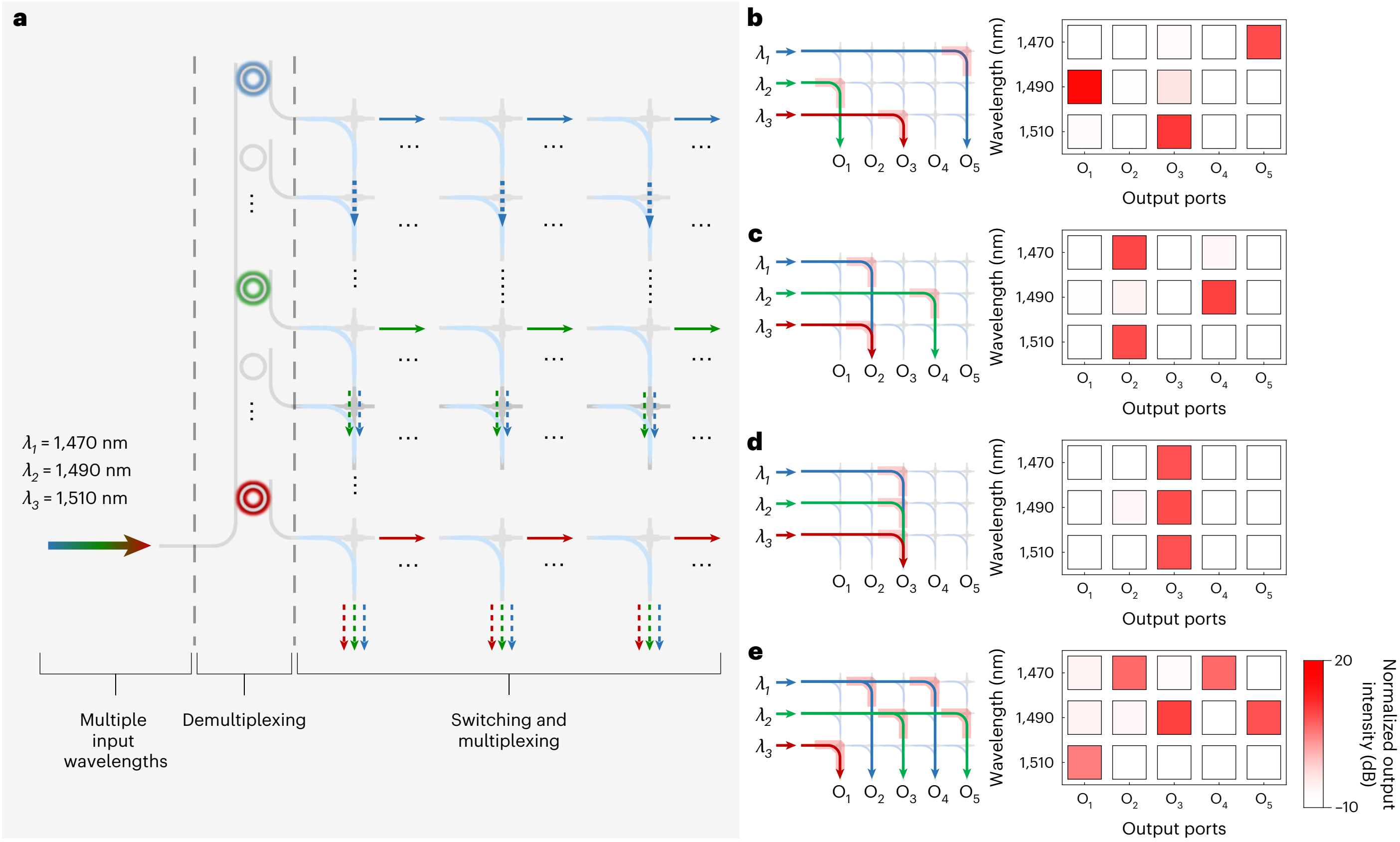

Fig. 4 | Demonstration of WSS. a, False-colour schematic of the working principle, which includes three parts: multiwavelength input (with λ_1 = 1,470 nm, λ_2 = 1,490 nm and λ_3 = 1,510 nm), demultiplexing (MRRs filtering different wavelengths to different channels) and switching and multiplexing (with the switch array routing and combining the light to horizontal output ports). **b**, Schematic of one-to-one switching (left) and the corresponding measured result (right). **c**–**e**, Schematics of switching (left) and the measured results (right) for two-to-one switching (**c**), multiple-to-one switching (**d**) and one-to-multiple switching (**e**). In **b**–**e**, output signal is normalized by the through port intensity (see Supplementary Section 7 for details).

various switching scenarios and multiple wavelengths in the S band. Our non-Hermitian hybrid architecture with InGaAsP integrated on top of silicon photonics is universal, providing opportunities for the exploration of gain materials with nonlinear responses in other visible and optical communication bands[34,35]. In addition, our non-Hermitian hybrid switch is compatible with electrically pumped platforms, which can be monolithically integrated with silicon photonics[36–38], for large-scale and high-dimensional information processing in optical communication and computing tasks.

Online content

Any methods, additional references, Nature Portfolio reporting summaries, source data, extended data, supplementary information, acknowledgements, peer review information; details of author contributions and competing interests; and statements of data and code availability are available at https://doi.org/10.1038/s41566-024-01579-9.

References

1. Lu, L. et al. 16×16 non-blocking silicon optical switch based on electro-optic Mach–Zehnder interferometers. *Opt. Express* **24**, 9295–9307 (2016).
2. Zhao, S. et al. 16×16 silicon Mach–Zehnder interferometer switch actuated with waveguide microheaters. *Photonics Res.* **4**, 202–207 (2016).
3. Qiao, L., Tang, W. & Chu, T. 32×32 silicon electro-optic switch with built-in monitors and balanced-status units. *Sci. Rep.* **7**, 42306 (2017).
4. Shen, Y. et al. Deep learning with coherent nanophotonic circuits. *Nat. Photonics* **11**, 441–446 (2017).
5. Sherwood-Droz, N. et al. Optical 4×4 hitless silicon router for optical Networks-on-Chip (NoC). *Opt. Express* **16**, 15915–15922 (2008).
6. Cheng, Q. et al. Ultralow-crosstalk, strictly non-blocking microring-based optical switch. *Photonics Res.* **7**, 155–161 (2019).
7. Cheng, Z. et al. On-chip silicon electro-optical modulator with ultra-high extinction ratio for fiber-optic distributed acoustic sensing. *Nat. Commun.* **14**, 7409 (2023).
8. Seok, T. J., Quack, N., Han, S., Muller, R. S. & Wu, M. C. Large-scale broadband digital silicon photonic switches with vertical adiabatic couplers. *Optica* **3**, 64–70 (2016).
9. Kim, D. U. Programmable photonic arrays based on microelectromechanical elements with femtowatt-level standby power consumption. *Nat. Photonics* **17**, 1089–1096 (2023).
10. Haffner, C. et al. Low-loss plasmon-assisted electro-optic modulator. *Nature* **556**, 483–486 (2018).
11. Haffner, C. et al. Nano–opto-electro-mechanical switches operated at CMOS-level voltages. *Science* **366**, 860–864 (2019).
12. Midolo, L., Schliesser, A. & Fiore, A. Nano-opto-electro-mechanical systems. *Nat. Nanotechnol.* **13**, 11–18 (2018).
13. Wonfor, A., Wang, H., Penty, R. V. & White, I. H. Large port count high-speed optical switch fabric for use within datacenters [invited]. *J. Opt. Commun. Netw.* **3**, A32–A39 (2011).
14. Stabile, R., Rohit, A. & Williams, K. A. Monolithically integrated 8×8 space and wavelength selective cross-connect. *J. Lightwave Technol.* **32**, 201–207 (2014).

15. Davenport, M. L. et al. Heterogeneous silicon/III–V semiconductor optical amplifiers. *IEEE J. Sel. Top. Quantum Electron.* **22**, 78–88 (2016).
16. Cheng, Q., Wonfor, A., Wei, J. L., Penty, R. V. & White, I. H. Monolithic MZI–SOA hybrid switch for low-power and low-penalty operation. *Opt. Lett.* **39**, 1449–1452 (2014).
17. Konoike, R. et al. SOA-integrated silicon photonics switch and its lossless multistage transmission of high-capacity WDM signals. *J. Lightwave Technol.* **37**, 123–130 (2019).
18. Matsumoto, T. et al. Hybrid-integration of SOA on silicon photonics platform based on flip-chip bonding. *J. Lightwave Technol.* **37**, 307–313 (2019).
19. Feng, L., El-Ganainy, R. & Ge, L. Non-Hermitian photonics based on parity–time symmetry. *Nat. Photonics* **11**, 752–762 (2017).
20. Zhao, H. et al. Non-Hermitian topological light steering. *Science* **365**, 1163–1166 (2019).
21. Liao, K. et al. On-chip integrated exceptional surface microlaser. *Sci. Adv.* **9**, eadf3470 (2023).
22. El-Ganainy, R., Makris, K. G., Christodoulides, D. N. & Musslimani, Z. H. Theory of coupled optical PT-symmetric structures. *Opt. Lett.* **32**, 2632–2634 (2007).
23. Guo, A. et al. Observation of $\mathcal{PT}$-symmetry breaking in complex optical potentials. *Phys. Rev. Lett.* **103**, 093902 (2009).
24. Rüter, C. E. et al. Observation of parity–time symmetry in optics. *Nat. Phys.* **6**, 192–195 (2010).
25. Ge, L., Makris, K. G. & Zhang, L. Optical fluxes in coupled $\mathcal{PT}$-symmetric photonic structures. *Phys. Rev. A* **96**, 023820 (2017).
26. Deng, H. & Khajavikhan, M. Parity–time symmetric optical neural networks. *Optica* **8**, 1328–1333 (2021).
27. Moiseyev, N. *Non-Hermitian Quantum Mechanics* (Cambridge Univ. Press, 2011).
28. Zhang, Z. et al. Ultrafast control of fractional orbital angular momentum of microlaser emissions. *Light Sci. Appl.* **9**, 179 (2020).
29. Sun, B. Q., Gal, M., Gao, Q., Tan, H. H. & Jagadish, C. On the nature of radiative recombination in GaAsN. *Appl. Phys. Lett.* **81**, 4368–4370 (2002).
30. Uzdin, R., Mailybaev, A. & Moiseyev, N. On the observability and asymmetry of adiabatic state flips generated by exceptional points. *J. Phys. A* **44**, 435302 (2011).
31. Doppler, J. et al. Dynamically encircling an exceptional point for asymmetric mode switching. *Nature* **537**, 76–79 (2016).
32. Goldzak, T., Mailybaev, A. A. & Moiseyev, N. Light stops at exceptional points. *Phys. Rev. Lett.* **120**, 013901 (2018).
33. Moiseyev, N. & Šindelka, M. Transfer of information through waveguides near an exceptional point. *Phys. Rev. A* **103**, 033518 (2021).
34. Liao, K. et al. Spintronics of hybrid organic–inorganic perovskites: miraculous basis of integrated optoelectronic devices. *Adv. Opt. Mater.* **7**, 1900350 (2019).
35. Roelkens, G. et al. III–V/silicon photonics for on-chip and intra-chip optical interconnects. *Laser Photon. Rev.* **4**, 751–779 (2010).
36. Fang, A. W. et al. Electrically pumped hybrid AlGaInAs-silicon evanescent laser. *Opt. Express* **14**, 9203–9210 (2006).
37. Liang, D., Huang, X., Kurczveil, G., Fiorentino, M. & Beausoleil, R. G. Integrated finely tunable microring laser on silicon. *Nat. Photonics* **10**, 719–722 (2016).
38. Huang, D. et al. High-power sub-kHz linewidth lasers fully integrated on silicon. *Optica* **6**, 745–752 (2019).

Methods

Sample fabrication

The fabrication flow of the III–V/Si hybrid photonic switch is shown in Extended Data Fig. 1. Thermal oxidation was first performed on the silicon-on-insulator (SOI) wafer to form a layer of SiO_2 on the top of silicon layer. Then the wafer was diced to chip scale, patterned via electron-beam lithography using the ZEP520A positive resist. After developing in o-xylene, the SiO_2 layer was dry-etched in inductively coupled plasma with CHF_3, and then the silicon layer was dry-etched via reactive-ion etching with SF_6/C_4F_8. The patterned sample was cleaned in *N*-methyl-2-pyrrolidone, acetone and isopropyl alcohol to remove the resist and other surface contaminants. Both the patterned SOI chip and the unpatterned III–V chip with an InGaAsP multi-quantum well and InP substrate were treated with O_2 plasma in the asher, for surface activation and further cleaning. The III–V chip was flipped and bonded with the SOI chip using a customized clamping tool, then annealed at 300 °C for 15–20 h. After the InP substrate had been removed by a 3:1 mixture of hydrochloric acid and water, the bonded hybrid chip was patterned via electron-beam lithography again with the alignment process, where hydrogen silsesquioxane solution in methyl isobutyl ketone was used as a negative resist (with a flowable oxide (FOX15) to methyl isobutyl ketone ratio of 2:3). The resist was developed in tetramethylammonium hydroxide solution (MFCD-26) and rinsed in deionized water. The InGaAsP multi-quantum well was later dry-etched with inductively coupled plasma in a mixture of BCl_3 and argon gas. Finally, a SiO_2 cladding was deposited via plasma-enhanced chemical vapour deposition.

Optical characterization

A schematic of the experimental set-up for optical characterization is shown in Extended Data Fig. 2. The input signal laser at 1,490 nm (or 1,470 nm/1,510 nm, repetition rate 10–1000 kHz, adjustable pulse width down to <10 ns) was electrically triggered by the pump laser (1,064 nm, tunable repetition rate at 10–150 kHz, pulse width ~7–20 ns depending on the pulse energy). Details of the working principles of this set-up are discussed in the following sections.

Pump beam. The pump laser was coupled into a fibre delay line through a fibre collimator, then coupled back to free space to another delay line for finer delay tuning. These two delay lines compensate the relative delay of the electrical triggering between the signal and the pump lasers. The pump beam was expanded and then attenuated using a variable neutral density filter. The pump pattern (only when measuring the large switch array) was generated by the SLM with a computer-generated hologram. A longpass dichroic mirror (1,180 nm cut-on wavelength), which reflects the pump beam but passes the signal beam, merges the input pump and signal beam, and filters out most of the pump light reflected from the sample surface. The objective (×10 or ×20, depending on the sample size) was used for both input and imaging.

Signal beam. The signal beam first passed through a half-wave plate that aligns its polarization with the input grating couplers on the integrated switching array for maximum input efficiency. The beam was then expanded and collimated using a pair of lenses, reflected by a polarizing beamsplitter, and focused onto the sample.

Imaging system. The imaging system consists of a CCD camera and a 1,490 nm bandpass filter (BPF) with a full-width at half-maximum of 12 nm (or a longpass filter, cut-on wavelength 1,350 nm) to filter out the pump light reflected from the sample surface. The polarizing beamsplitter also blocks the vertically polarized input light so that the intensity of the scattered light from the input beam can be minimized during imaging of the output grating couplers.

Spectrum characterization. Light exiting the output grating couplers from the chip was redirected to the spectrum-characterization system using a flip mirror (FM1), and then focused at the input slit of the monochromator using a ×5 objective. The spectrum was collected by the InGaAs detector connected with the lock-in amplifier, with an optical chopper applied along the optical path to maximize the signal-to-noise ratio. An iris (Iris 1) was placed in the image plane so that the desired output port can be selected in the camera and spatially filtered before measurement of the spectrum.

Time-response measurement. The light collected from the sample was redirected via another flip mirror (FM2) for time-response measurement. Here the light is also selected and filtered using another iris (Iris 2) on the image plane, monitoring by another CCD camera. When flip mirror FM3 was laid down, the light was split into two paths by a beamsplitter, and attenuated with a pair of variable neutral density filters to the single-photon level. The downward path measures the signal light from the output grating couplers on the sample, with a 1,490 nm BPF in front of the single-photon avalanche diode detector (SPAD1). The other path measures the pump light with a 1,064 nm BPF in front of the detector SPAD2. Both detectors were connected with the event timer, which was electrically triggered by the pump laser so that the histogram of the relative delay between the two optical pulses and the electrical signal can be measured. Further details are discussed in Supplementary Section 3.

Data availability

Source data are provided with this paper. All other data that support other findings of this study are available from the corresponding author upon reasonable request.

Acknowledgements

We acknowledge support from the Army Research Office (ARO) (W911NF-21-1-0148 and W911NF-22-1-0140), the Office of Naval Research (ONR) (N00014-23-1-2882) and the National Science Foundation (NSF) (ECCS-2023780, DMR-2117775, DMR-2326698 and DMR-2326699). This work was carried out in part at the Singh Center for Nanotechnology, which is supported by the NSF National Nanotechnology Coordinated Infrastructure Program under grant no. NNCI-1542153.

Author contributions

L.F. and X.F. designed the experiment. X.F., T.W., Z.G., L.G. and L.F. designed the photonic switch. X.F., T.W. and L.G. constructed the theoretical model. X.F. performed numerical simulations and fabricated the sample. X.F., T.W., Z.G., H.Z. and Y.Z. performed the measurements. X.F. and S.W. performed the data processing. X.F., S.W., L.G. and L.F. prepared the manuscript. All the authors contributed to the discussions.

Competing interests

The authors declare no competing interests.

Additional information

Extended data is available for this paper at https://doi.org/10.1038/s41566-024-01579-9.

Supplementary information The online version contains supplementary material available at https://doi.org/10.1038/s41566-024-01579-9.

Correspondence and requests for materials should be addressed to Liang Feng.

Peer review information *Nature Photonics* thanks the anonymous reviewers for their contribution to the peer review of this work.

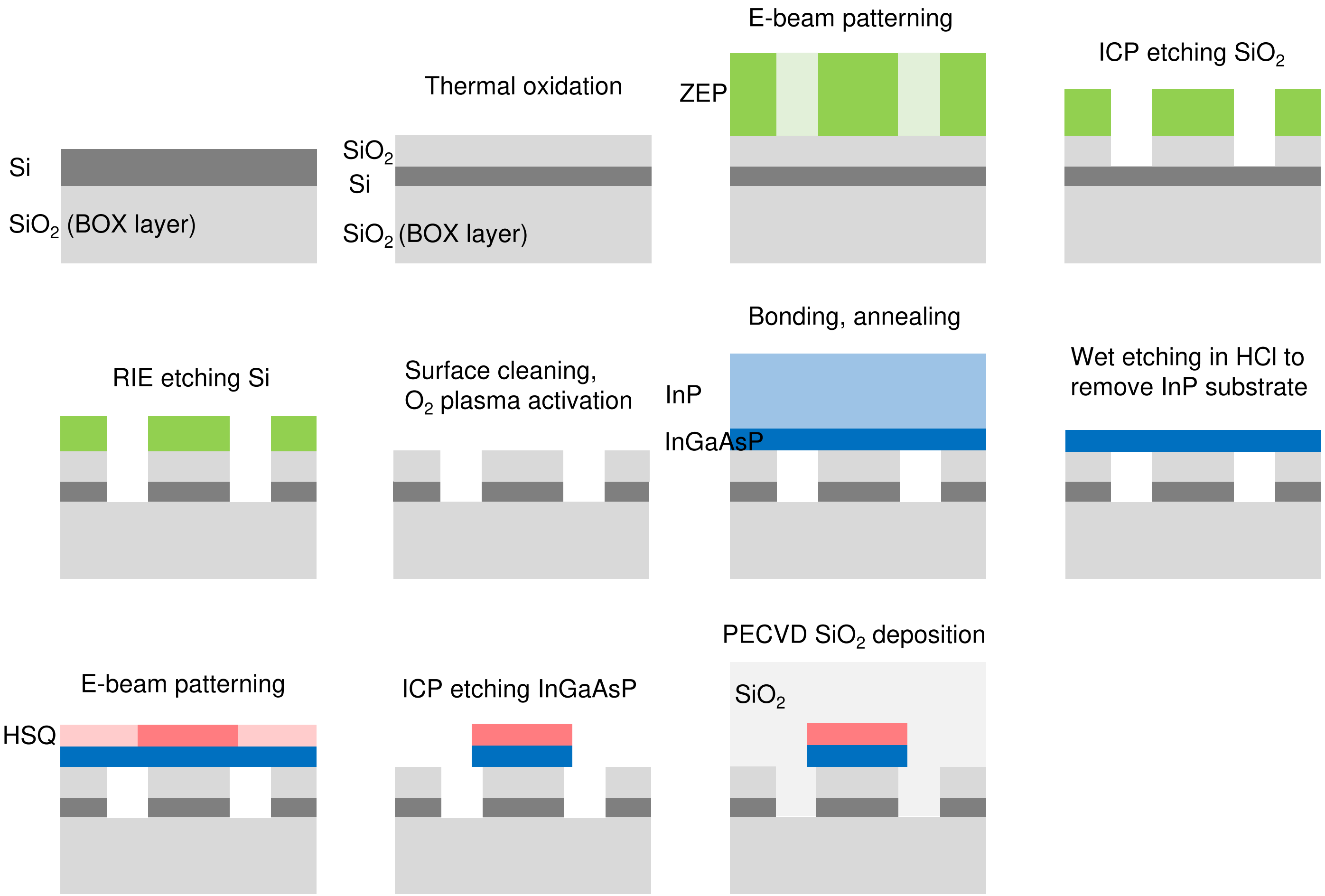

Extended Data Fig. 1 | Fabrication flow of the III-V/Si hybrid photonic switch.

https://doi.org/10.1038/s41566-024-01579-9

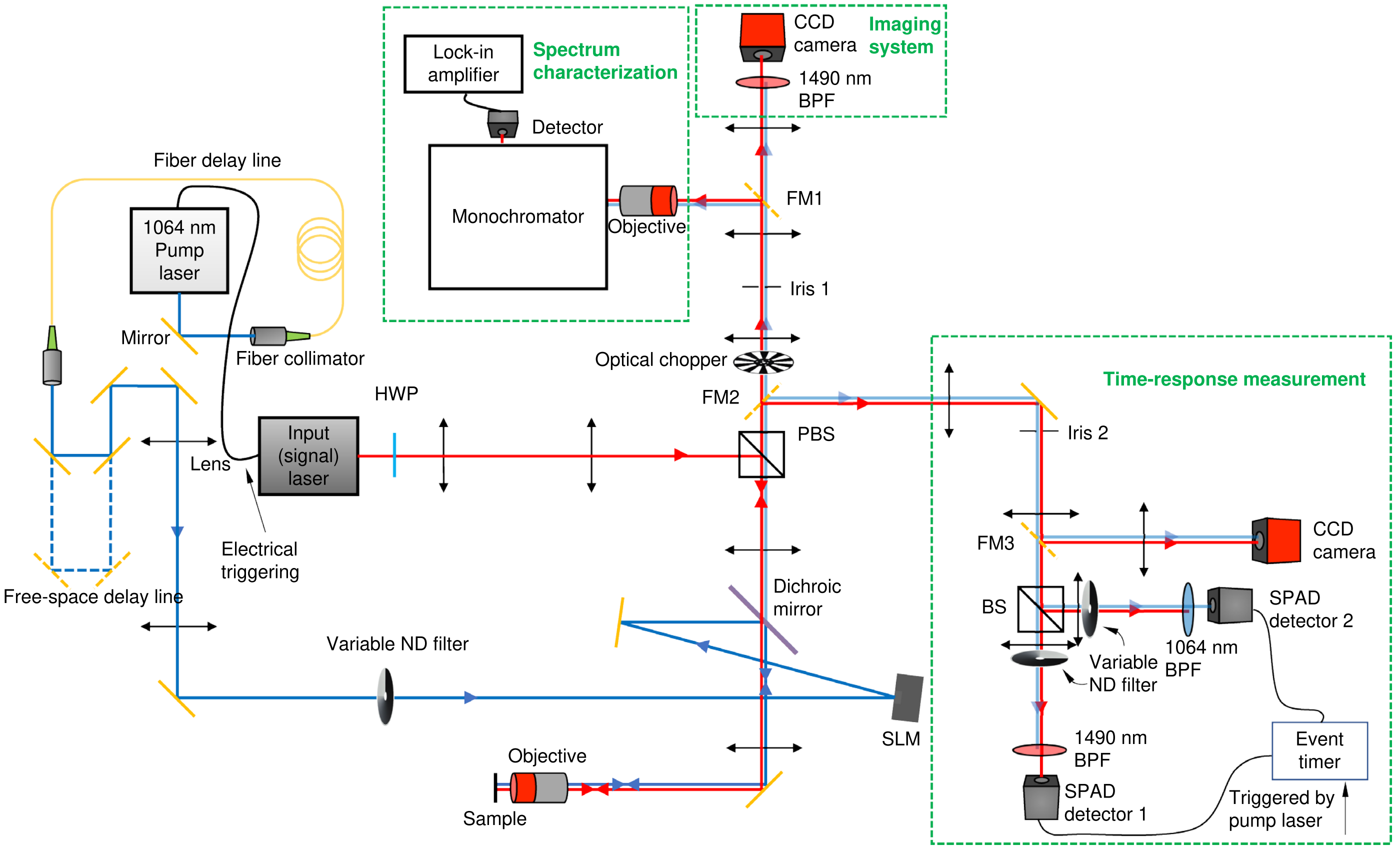

Extended Data Fig. 2 | Schematic of experimental setup. Blue line: pump beam. Red line: signal beam. ND: neutral density. HWP: half-wave plate. PBS: polarizing beamsplitter. BPF: bandpass filter. FM: flip mirror. BS: beamsplitter. SPAD: single photon avalanche diode.